

# Electrostatic Covalent Organic Frameworks as On-Demand Molecular Traps for High-Energy Li Metal Battery Electrodes

Kyeong-Seok Oh, Sodam Park, Jae-Seung Kim, Ying Yao, Jung-Hui Kim, Jia Guo,\* Dong-Hwa Seo,\* and Sang-Young Lee\*



Cite This: *ACS Energy Lett.* 2023, 8, 2463–2474



Read Online

ACCESS |



Metrics & More

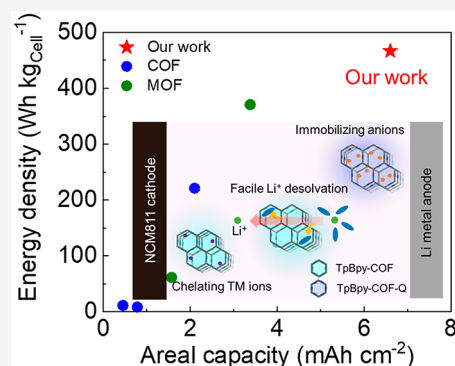


Article Recommendations



Supporting Information

**ABSTRACT:** Regulating electrostatic interactions between charged molecules is crucial for enabling advanced batteries with electrochemical reliability. To address this issue, herein, we present a class of electrostatic covalent organic frameworks (COFs) as on-demand molecular traps for high-energy-density Li metal batteries (LMBs). A bipyridine-based COF and its quaternized derivative are synthesized and incorporated into  $\text{LiNi}_{0.8}\text{Co}_{0.1}\text{Mn}_{0.1}\text{O}_2$  (NCM811) cathodes and Li metal protective layers, respectively. These COF molecular traps are effective in chelating transition metal ions dissolved from the cathodes, enhancing  $\text{Li}^+$  desolvation, suppressing solvent decomposition, and immobilizing anions of electrolytes. The resulting LMB with the COF molecular traps fully utilizes the theoretical specific capacity of NCM811 at cathodes and allows stable Li plating/stripping at anodes. A pouch-type LMB full cell with the COF molecular traps provides high gravimetric/volumetric energy densities ( $466.7 \text{ Wh kg}_{\text{cell}}^{-1}/1370.1 \text{ Wh L}_{\text{cell}}^{-1}$ ) under a constrained cell configuration, exceeding those of previously reported Li metal batteries based on porous crystalline frameworks.



The development of high-energy-density batteries with electrochemical sustainability has attracted considerable attention owing to the potential growth of smart portable electronics, electric vehicles (EVs), grid-scale energy storage systems (ESSs), and the Internet of Things.<sup>1,2</sup> Among several battery systems explored to date, Li metal batteries (LMBs) comprising thin Li metal anodes and high-capacity cathodes have been investigated as a promising power source to fulfill this high-energy-density requirement.<sup>3,4</sup>

Previous studies on LMBs have mostly focused on addressing the limitations of Li metal anodes, including low Coulombic efficiency (CE), interfacial side reactions between Li and electrolytes, dendritic Li growth, formation of dead Li, and uncontrollable volume changes.<sup>5–7</sup> In addition to this research aimed at enhancing Li metal anodes, significant attention should be simultaneously devoted to high-capacity cathodes to achieve practical high-energy-density LMBs. However, Ni-rich cathode materials, as an example of one of the most spotlighted materials for LMBs, are plagued with the dissolution of transition metal (TM) ions (e.g.,  $\text{Ni}^{2+}$  and  $\text{Mn}^{2+}$ ), which impairs the structural stability of the cathode materials.<sup>8–10</sup> Furthermore, the dissolved TM ions induce electrolyte decomposition<sup>10</sup> and diffuse toward Li metal

anodes, resulting in the formation of undesired passivation layers.<sup>8,11</sup>

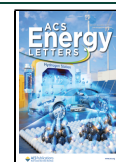
The development of advanced electrolytes has been extensively investigated as an effective and popular approach to resolve the aforementioned challenges, focusing on synthesis and engineering of new salts/solvents and control of coordination chemistry.<sup>12,13</sup> However, the electrolytes should simultaneously meet the different chemical/electrochemical requirements of Li metal anodes and high-capacity cathodes while providing high ionic conductivity over a wide range of temperatures. Moreover, interfacial side reactions between the electrolytes and electrodes often generate unwanted by-products during charge/discharge cycling.<sup>14,15</sup>

In contrast to the approaches described above, our focus is on regulating electrostatic interactions between charged molecules during battery operation. Driven by complex

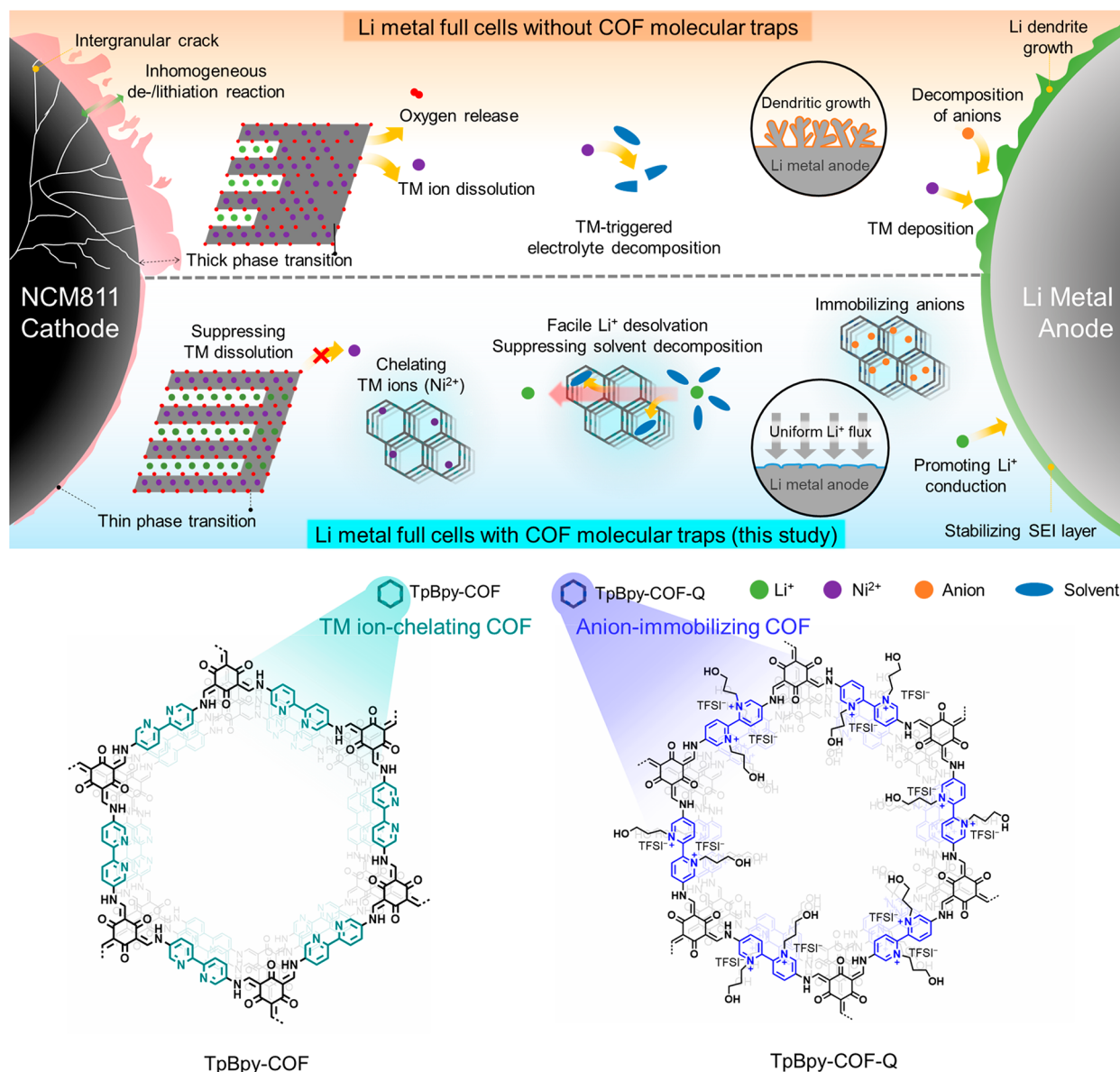
Received: March 20, 2023

Accepted: May 2, 2023

Published: May 4, 2023



**Scheme 1. Advantageous Effects of On-Demand COF Molecular Traps on the LMB Electrodes, and the Chemical Structures of the  $\beta$ -Ketoenamine-Linked COF (TpBpy-COF) for the NCM811 Cathode and the Postquaternized TpBpy-COF (TpBpy-COF-Q) for the Li Metal Anode**



charge/discharge reactions, these intermolecular electrostatic interactions tend to continuously evolve, which eventually affects redox stability at electrodes and cycling retention. To achieve this goal, herein, we present an on-demand molecular trap strategy based on electrostatic covalent organic frameworks (COFs) with electrode-customized molecular structures. COFs are chosen as the platform material for these molecular traps due to their highly porous structures with chemical diversity,<sup>16–20</sup> which can effectively maximize the advantageous effects of the molecular traps. The COF molecular traps are rationally designed to control intermolecular electrostatic interactions in both Li metal anodes and  $\text{LiNi}_{0.8}\text{Co}_{0.1}\text{Mn}_{0.1}\text{O}_2$  (NCM811) cathodes simultaneously. To this end, first, 1,3,5-triformyl phloroglucinol (Tp) is condensed with 5,5'-diamino-2,2'-bipyridine (Bpy) via the reversible aldimine reaction and irreversible enol-to-keto transformation to obtain  $\beta$ -ketoenamine-linked COF (TpBpy-COF). Subsequently, TpBpy-COF is subjected to a postquaternization process to obtain highly

ionized skeletons (TpBpy-COF-Q) with linear propanol side chains. Owing to its electrostatic repulsion, the postquaternized TpBpy-COF-Q can be exfoliated into dispersible nanosheets, thus effectively exposing its functional sites.

The synthesized TpBpy-COF is incorporated into a  $\text{LiNi}_{0.8}\text{Co}_{0.1}\text{Mn}_{0.1}\text{O}_2$  (NCM811) cathode as a molecular trap to electrostatically attract TM ions dissolved from NCM811. Meanwhile, the TpBpy-COF-Q is introduced as a constituent of the artificial solid electrolyte interphase (SEI) layer that can be directly fabricated on a Li metal anode using a simple and scalable ultraviolet (UV)-curing-assisted printing process.<sup>21</sup> The TpBpy-COF-Q contributes to immobilizing anions of the liquid electrolytes through electrostatic attraction, thus enhancing  $\text{Li}^+$  transport (leading to a high  $\text{Li}^+$  transference number ( $t_{\text{Li}^+}$ )). Moreover, both COF molecular traps enable dipole (COF)–dipole (solvent) interaction with the  $\text{Li}^+$  solvation sheath of liquid electrolytes, thereby lowering  $\text{Li}^+$  desolvation energy and suppressing direct contact of solvents

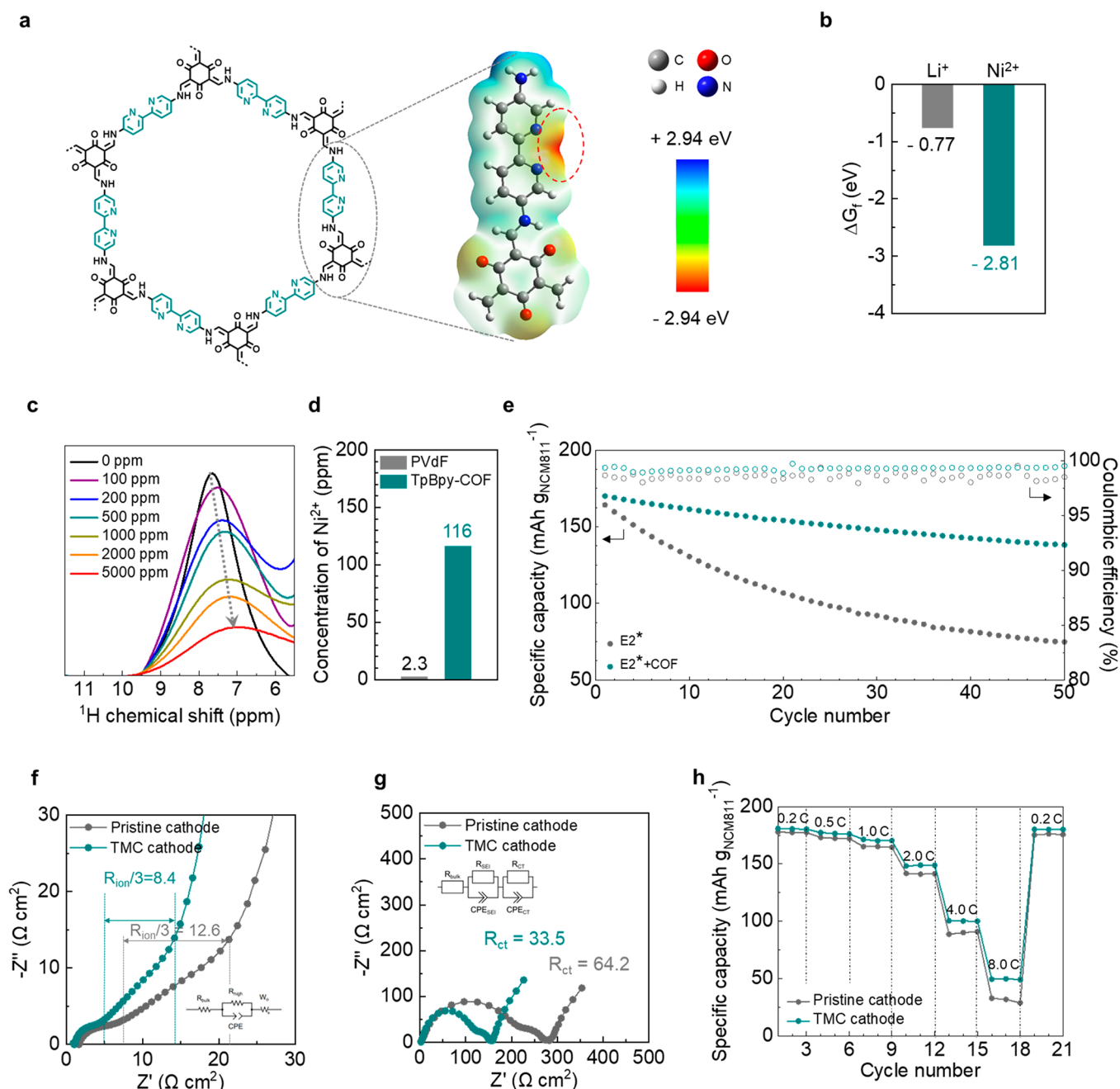


**Figure 1.** TpBpy-COF molecular trap for the NCM811 cathode: Chelating TM ions and enhancing  $\text{Li}^+$  desolvation. (a) MESP map of the H-terminated TpBpy-COF motif. The red and blue represent the electron-rich and electron-deficient regions, respectively. The red-dashed area indicates the region with the lowest ESP value. (b) Comparison of the  $\Delta G_f$  of  $\text{Li}^+$ -bipyridine and  $\text{Ni}^{2+}$ -bipyridine complexes. (c) Solid-state  $^1\text{H}$  NMR spectra of the TpBpy-COF specimens that were soaked in the  $\text{Ni}^{2+}$ -containing solution as a function of the  $\text{Ni}^{2+}$  concentration. (d) Concentration of  $\text{Ni}^{2+}$  captured by the PVdF and TpBpy-COF films (obtained from the ICP-OES analysis). (e) Cycling performance of the NCM811 cathode/Li metal anode half cells containing the  $\text{E}2^*$  and  $\text{E}2^* + \text{COF}$  at a charge/discharge current density of 1.0 C/1.0 C. Nyquist plots of the symmetric cathodes (NCM811 cathode||NCM811 cathode): (f) 0% SOC and (g) 50% SOC, wherein the insets show the corresponding equivalent circuit models.<sup>28,34</sup> (h) Rate capability of the TMC cathode (vs pristine cathode), in which the discharge current density was varied from 0.2 to 8.0 C at a fixed charge current density of 0.2 C.

with electrodes. These advantageous roles of the on-demand COF molecular traps are conceptually depicted in Scheme 1.

Owing to the coupled effects of the TpBpy-COF and TpBpy-COF-Q as on-demand molecular traps, the resulting LMB (hereinafter, denoted as COF-LMB) full cell enables stable Li plating/stripping cyclability at the Li metal anodes and fully utilizes the theoretical specific capacity of NCM811 ( $\sim 208 \text{ mAh g}_{\text{NCM811}}^{-1}$ )<sup>3</sup> over a wide range of areal mass

loadings (even at  $31.6 \text{ mg cm}^{-2}$ ). Furthermore, we fabricate a pouch-type COF-LMB full cell to explore the practical viability of the COF molecular traps. Under a constrained cell configuration (NCM811 cathode ( $6.6 \text{ mAh cm}^{-2}$ )||Li metal anode ( $10.0 \text{ mAh cm}^{-2}$ ) and lean electrolyte ( $2.3 \text{ g Ah}^{-1}$ )), the full cell provides high gravimetric/volumetric energy densities ( $466.7 \text{ Wh kg}_{\text{cell}}^{-1}/1370.1 \text{ Wh L}_{\text{cell}}^{-1}$ ) and stable cycling performance, which exceed those of previously reported full



cells based on porous crystalline frameworks (including metal-organic frameworks (MOFs) as well as COFs).

To exploit COFs as molecular traps for LMB cells, the COFs should not be dissolved in liquid electrolytes but should exhibit a high surface area to promote intermolecular interaction between charged molecules. Taking these requirements into account, we rationally designed the structure of COF molecular traps. TpBpy-COF was solvothermally synthesized using acetic acid as a catalyst. The catalyst induced the interconversion of bipyridine from its *trans*- to *cis*-form at the strut of its framework.<sup>22,23</sup> Additionally, the eclipsed stacking of the layered structures enforced the planar configuration of *cis*-bipyridine to effectively chelate TM ions dissolved from NCM811. Meanwhile, as the tight-layered stacking was weakened during the postsynthesis, the *cis*-to-*trans* transformation of bipyridine was energetically favorable to enable the dual quaternization with linear propanol chains, thereby conferring an exceptionally high ionization degree for the TpBpy-COF-Q. The structural characterization of the synthesized TpBpy-COF and TpBpy-COF-Q was conducted using the Fourier transform infrared (FT-IR) spectra, solid-state <sup>13</sup>C nuclear magnetic resonance (<sup>13</sup>C NMR) spectra, X-ray photoelectron spectroscopy (XPS) spectra, scanning electron microscopy (SEM), transmission electron microscopy (TEM) images, and powder X-ray diffraction (PXRD) analysis (Figures S1–S7 and Tables S1–S4).

The porous structure of the TpBpy-COF and TpBpy-COF-Q, which plays a viable role in enabling the TpBpy-COF and TpBpy-COF-Q as electrode-customized molecular traps, was analyzed using N<sub>2</sub> sorption measurement at 77 K (Figure S8). This result revealed that both TpBpy-COF and TpBpy-COF-Q exhibited the type-IV adsorption isotherms, indicating a mesoporous structure. Meanwhile, we observed that both TpBpy-COF and TpBpy-COF-Q stably maintained their crystalline structure without any loss in the weight after storage in a liquid electrolyte (1 M LiPF<sub>6</sub> in EC/EMC = 3/7 (v/v) with 10 wt % FEC, 1 wt % VC) at 45 °C for 1 week (Figure S9), exhibiting that these COFs are not dissolved in the electrolyte.

The TM ion-chelating ability of TpBpy-COF was simulated using a H-terminated TpBpy-COF motif. The electrostatic potential (ESP) of the TpBpy-COF was calculated using the molecular electrostatic potential (MESP) analysis (Figure 1a; see the Simulation details). The lowest ESP value was observed for the bipyridine group of the TpBpy-COF. To verify TM ion-chelating ability, the electrostatic interaction (Figure S10) between the functional groups of the TpBpy-COF and various cations (Li<sup>+</sup>, Ni<sup>2+</sup>, and Mn<sup>2+</sup>) was calculated by comparing the Gibbs free energy of formation ( $\Delta G_f$ ). Figure 1b shows that the  $\Delta G_f$  (−2.81 eV) of Ni<sup>2+</sup>-bipyridine (from the TpBpy-COF) complex was lower than that of the Li<sup>+</sup>-bipyridine complex ( $\Delta G_f$  = −0.77 eV), indicating that the dissolved Ni<sup>2+</sup> can strongly interact with the TpBpy-COF. In addition, another TM ion (i.e., Mn<sup>2+</sup>) interacted with the TpBpy-COF ( $\Delta G_f$  = −1.61 eV, Figure S10b). This theoretical result indicated that the bipyridine site of the TpBpy-COF can chelate TM ions (such as Ni<sup>2+</sup> and Mn<sup>2+</sup>) through electrostatic interaction, thus mitigating the dissolution of TM ions from NCM811, which results in the depression of disproportionation at the cathode surface.<sup>8,24</sup>

Based on the above-described theoretical understanding, the chelation of Ni<sup>2+</sup> by the TpBpy-COF was experimentally investigated. For this purpose, a TpBpy-COF specimen was

prepared as a model sample, and then, it was soaked in a NiCl<sub>2</sub>-containing aqueous solution, in which the Ni<sup>2+</sup> concentration was varied from 100 to 5000 ppm. Subsequently, the soaked TpBpy-COF was subjected to solid-state <sup>1</sup>H NMR analysis (Figure 1c). The <sup>1</sup>H NMR analysis revealed the upward shift and gradual broadening of the characteristic peak of bipyridine at 7.7 ppm<sup>24</sup> as the Ni<sup>2+</sup> concentration increased, confirming the chelation of Ni<sup>2+</sup> by the TpBpy-COF. This TM ion-chelating capability of the soaked TpBpy-COF was quantitatively verified using inductively coupled plasma optical emission spectrometry (ICP-OES). The amounts of TM ions trapped by the TpBpy-COF specimen were estimated to be 116.0 (Ni<sup>2+</sup>) and 194.5 (Mn<sup>2+</sup>) ppm, respectively, which were higher than those (2.3 (Ni<sup>2+</sup>) and 16.3 (Mn<sup>2+</sup>) ppm) of a polyvinylidene fluoride (PVdF) specimen that has been widely used as a commercial cathode binder and those (4.5 (Ni<sup>2+</sup>) and 9.7 (Mn<sup>2+</sup>) ppm) of an azine-linked COF specimen<sup>25,26</sup> chosen as a COF analogue that has a similar backbone structure without pyridine moieties. For this comparison, the PVdF and azine-linked COF specimens were prepared to show the same dimensions and weights as those of the TpBpy-COF (Figures 1d and S11). This result confirms the viable role of the TpBpy-COF in chelating TM ions.

The effect of the TpBpy-COF on electrolyte stability was investigated, in which electrolyte #1 (1.0 M lithium hexafluorophosphate (LiPF<sub>6</sub>) + 0.6 M lithium bis(trifluoromethanesulfonyl) imide (LiTFSI) in ethylene carbonate (EC)/ethyl methyl carbonate (EMC) = 3/7 (v/v) with 10 wt % fluoroethyl carbonate (FEC), 1 wt % vinylene carbonate (VC), denoted as E1) and electrolyte #2 (1.0 M LiPF<sub>6</sub> + 0.3 M Ni(TFSI)<sub>2</sub> in EC/EMC = 3/7 (v/v) with 10 wt % FEC, 1 wt % VC, denoted as E2) were used (Figure S12). It was observed that the TpBpy-COF plays a viable role in suppressing the catalytic Ni<sup>2+</sup>-driven parasitic side reactions in NCM811-containing cells. This advantageous effect of the TpBpy-COF was further verified by analyzing the NMR spectra of E2, E2\*, and E2\* + COF (Figure S13). As a model study to confirm this beneficial effect of the TpBpy-COF on the electrolyte stability, the cycling performance of the NCM811 cathode (areal capacity = 3.8 mAh cm<sup>−2</sup>)||Li metal anode (areal capacity = 20 mAh cm<sup>−2</sup> corresponding to a thickness of 100 μm) half cells was investigated at 45 °C, which was selected to expedite the detrimental effects caused by the dissolution of TM ions (Figure 1e).<sup>10</sup> Compared to the control cell with E2\* (46% after 50 cycles), the cell with E2\* + COF exhibited a higher cycle retention (81% after 50 cycles), demonstrating the beneficial contribution of TpBpy-COF to the cycling performance of the electrolyte through the chelation of TM ions dissolved in the electrolytes.

In addition to the TM ion-chelating capability of the TpBpy-COF, its influence on Li<sup>+</sup> desolvation was investigated. Upon the addition of the TpBpy-COF, the desolvation energy of Li(EC)<sub>4</sub><sup>+</sup> was reduced to 0.23 eV (from 0.48 eV for the pristine liquid electrolyte) (Figure S14). This result indicates that the incorporated TpBpy-COF can attract EC molecules from Li(EC)<sub>4</sub><sup>+</sup> via dipole-dipole interaction (Figure S15), which is in agreement with the result of a previous study<sup>27</sup> that reported the facile Li<sup>+</sup> desolvation in carbonate-based electrolytes by the addition of ethidium bromide COF:NO<sub>3</sub>.

Next, we investigated the optimal TpBpy-COF content in the NCM811 cathode (NCM811/carbon black conductive additive/PVdF binder = 90/5/5 (w/w/w) and high mass



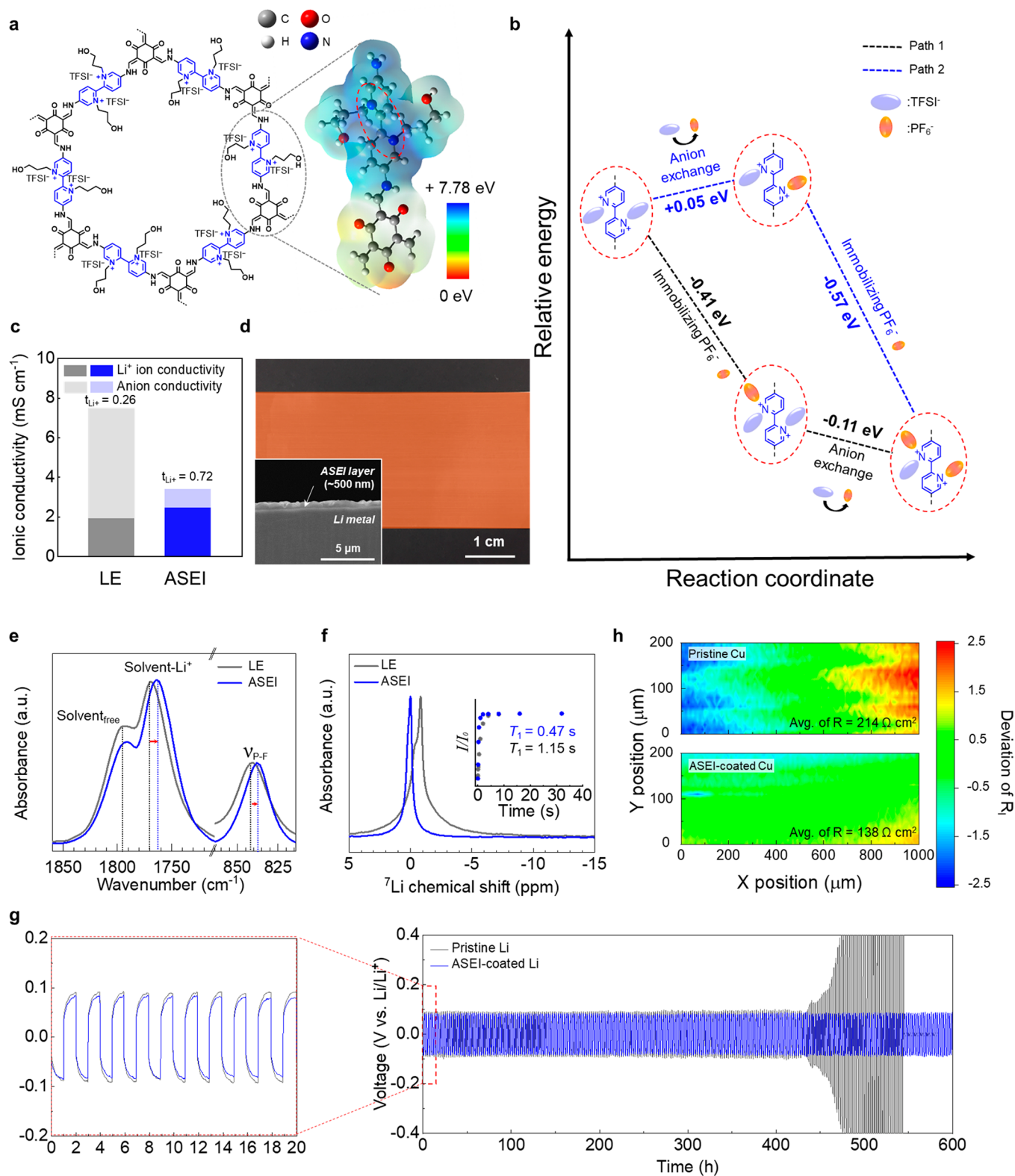


**Figure 2.** TpBpy-COF-Q molecular trap for the Li metal anode: Stabilization of Li metal anodes via anion immobilization. (a) MESP map of the TpBpy-COF-Q motif. The blue color represents the high ESP values (assigned to the electron-deficient region), while the red-dashed area indicates the region with the highest ESP value. (b) Schematic describing the mechanism of  $\text{PF}_6^-$  immobilization by TpBpy-COF-Q. (c)  $\text{Li}^+$  conductivity of the model ASEI layer (vs LE). (d) A photograph of the ASEI-coated Li metal foil. Inset is a cross-sectional SEM image of the ASEI layer on the Li metal foil. (e) FT-IR spectra and (f) solid-state  $^7\text{Li}$  NMR spectra of the model ASEI (vs LE). Inset shows the inversion-recovery plots obtained from the solid-state  $^7\text{Li}$  NMR analysis. (g) Voltage profiles of the Li||Li symmetric cells with the ASEI-coated Li metal (vs pristine Li metal) at a current density of  $1 \text{ mA cm}^{-2}$  and capacity of  $1 \text{ mAh cm}^{-2}$ . (h) LEIS analysis of the ASEI-coated Cu (vs pristine Cu) after five Li plating/stripping cycles.

loading of NCM811 ( $31.6 \text{ mg cm}^{-2}$  that corresponds to an areal capacity of  $6.6 \text{ mAh cm}^{-2}$ ). By monitoring the change in the specific discharge capacity ( $C_{\text{sp}}$ ) of NCM811 as a function of the TpBpy-COF content, we found that the suitable TpBpy-COF content in the cathode was 4 wt % (Figure S16).

The NCM811 cathode with the optimal TpBpy-COF content of 4 wt % (hereinafter, denoted as the TMC cathode) was characterized in detail. There was no significant difference in the thickness of the pristine and TMC cathodes ( $\sim 100 \text{ }\mu\text{m}$ , which corresponds to an areal capacity of  $6.6 \text{ mAh cm}^{-2}$ ), indicating that incorporation of the TpBpy-COF did not affect the resulting cathode structure. (Figure S17). Additionally, the energy-dispersive X-ray spectroscopy (EDS) analysis of the TMC cathode (Figure S17, right) showed the homogeneous distribution of the nitrogen (N) element (originating from the TpBpy-COF) throughout the entire region of the examined cathode, revealing the uniform dispersion of the TpBpy-COF. Meanwhile, the TMC cathode stably maintained a high electrode density ( $\sim 3.0 \text{ g cm}^{-3}$ )<sup>3</sup> over a wide range of areal mass loadings (Figure S18). This result indicates that incorporating the TpBpy-COF as a molecular trap exerts no significant effect on the structure of the TMC cathode.

The effect of TpBpy-COF on the ion-transport phenomena inside the cathodes was investigated by the electrochemical impedance spectroscopy (EIS) analysis of symmetric cathodes (NCM811 cathode||NCM811 cathode). At a state of charge (SOC) of 0%, the  $45^\circ$  slope in the low-frequency region, which represents ionic resistance ( $R_{\text{ion}}$ )/3 (estimated from transmission line model cylindrical pores), indicates the ionic resistance inside electrolyte-filled cathodes.<sup>28</sup> Compared to the pristine cathode ( $12.6 \text{ }\Omega \text{ cm}^2$ ), the TMC cathode exhibited a lower  $R_{\text{ion}}/3$  ( $8.4 \text{ }\Omega \text{ cm}^2$ ) (Figure 1f), indicating the advantageous role of the uniformly dispersed TpBpy-COF in facilitating ion conduction in the cathode. In addition, the charge-transfer resistance ( $R_{\text{ct}}$ ) of the TMC cathode ( $33.5 \text{ }\Omega \text{ cm}^2$ ) at 50% SOC was lower than that of the control cathode ( $64.2 \text{ }\Omega \text{ cm}^2$ ) (Figure 1g), which was ascribed to the enhanced  $\text{Li}^+$  desolvation enabled by the TpBpy-COF (as previously described in Figure S14). Consequently, the TMC cathode exhibited higher capacities than the pristine cathode over a broad range of discharge current densities (Figure 1h).

Free anions such as  $\text{PF}_6^-$  in liquid electrolytes often induce ion concentration polarization and nonuniform Li plating/stripping on Li metals.<sup>5–7</sup> Figure 2a indicates that the TpBpy-COF-Q exhibited the highest ESP (7.78 eV) near the bipyridinium groups, which possessed positively charged nitrogen atoms. This cationic repeating framework of the TpBpy-COF-Q plays a vital role in immobilizing anions (here,  $\text{PF}_6^-$ ) of liquid electrolytes via electrostatic attraction.

The immobilization mechanism of  $\text{PF}_6^-$  by the TpBpy-COF-Q was investigated using DFT calculation, which involved two steps: (1) immobilization of  $\text{PF}_6^-$  (Gibbs free energy to trap  $\text{PF}_6^-$ ,  $\Delta G_{\text{t}}$ ) and (2) anion exchange from TFSI<sup>−</sup> to  $\text{PF}_6^-$  (Gibbs free energy of exchange,  $\Delta G_{\text{e}}$ ), in which the TFSI<sup>−</sup> already exists as a counteranion in the TpBpy-COF-Q. Figure 2b indicates the spontaneity of the immobilization of  $\text{PF}_6^-$  in the vicinity of the TpBpy-COF-Q ( $\Delta G_{\text{t}} = -0.41 \text{ eV}$ , path 1). Subsequently, the TFSI<sup>−</sup> in the TpBpy-COF-Q can be exchanged with  $\text{PF}_6^-$ , which is energetically favorable ( $\Delta G_{\text{e}} = -0.11 \text{ eV}$ ). Meanwhile, for path 2, first, the TFSI<sup>−</sup> of the TpBpy-COF-Q was exchanged with the  $\text{PF}_6^-$  in the electrolyte, which could occur upon exposure to thermal perturbation because the  $\Delta G_{\text{e}}$  ( $= +0.05 \text{ eV}$ ) was relatively small.

Subsequently, additional  $\text{PF}_6^-$  can be captured by the TpBpy-COF-Q ( $\Delta G_{\text{t}} = -0.57 \text{ eV}$ ). In addition to the aforementioned paths 1 and 2, other paths (represented by paths 3 and 4) could be suggested (Figure S19). This theoretical consideration demonstrates that the immobilization of  $\text{PF}_6^-$  by the TpBpy-COF-Q was facilitated by their strong intermolecular electrostatic interaction.

The TpBpy-COF-Q described above was incorporated in an artificial SEI (denoted as ASEI) layer of a Li metal anode. The ASEI consisted of the TpBpy-COF-Q, the UV-irradiation-cured ethoxylated trimethylolpropane triacrylate (ETPTA) polymer matrix acting as a mechanical framework, and a liquid electrolyte. From the measurement of ionic conductivity of the ASEI as a function of the TpBpy-COF-Q/ETPTA composition ratio, an optimal TpBpy-COF-Q/ETPTA composition ratio was estimated to be 80/20 (w/w) (Figure S20). In addition, the high zeta potential and energy-dispersive X-ray spectroscopy (EDS) mapping images of the ASEI with the optimal composition ratio showed the uniform dispersion state of the TpBpy-COF-Q in the ASEI (Figure S21).

The ionic conductivity of the ASEI film was examined as a function of the temperature and compared to that of the liquid electrolyte (abbreviated as LE) (Figure S22). Despite having marginally lower ionic conductivity compared to the LE, the ASEI film exhibited a lower activation energy for ion conduction ( $E_{\text{a}}$ , obtained from the Arrhenius equation). Moreover, the  $t_{\text{Li}^+}$  (Figure S23a–d and Table S5) of the ASEI film was observed to increase ( $t_{\text{Li}^+} = 0.72$  vs  $0.26$  for the LE). Consequently, the ASEI film exhibited a higher  $\text{Li}^+$  conductivity ( $\sigma_{\text{Li}^+} = 2.45 \text{ mS cm}^{-1}$ , defined as ion conductivity multiplied by  $t_{\text{Li}^+}$ ) than the LE ( $\sigma_{\text{Li}^+} = 1.95 \text{ mS cm}^{-1}$ ) (Figure 2c). To further elucidate this anion immobilization enabled by the TpBpy-COF-Q, a control ASEI film with the TpBpy-COF was prepared, and its  $t_{\text{Li}^+}$  was measured (Figure S23e,f). There was no significant difference in  $t_{\text{Li}^+}$  between the control ASEI ( $t_{\text{Li}^+} = 0.27$ ) and LE ( $0.26$ ) (Table S5). This result demonstrates a viable role of the postquaternization of the COF in achieving anion immobilization, thereby enabling the TpBpy-COF-Q as a customized molecular trap for Li metal anodes. Based on this understanding of the model samples, the ASEI was introduced directly onto a Li metal foil using the UV-curing-assisted printing process,<sup>21,29,30</sup> and the resulting ASEI thin layer (thickness  $\approx 500 \text{ nm}$ ) was evenly deposited over a wide area on the Li metal foil, indicating its scalability for fabrication (Figures 2d and S24).

The anion immobilization in the ASEI layer by the TpBpy-COF-Q was further elucidated using spectroscopic analysis. The FT-IR spectra (Figure 2e) of the ASEI layer revealed a downshift in the characteristic vibration peak of the P–F bond ( $841 \text{ (LE)} \rightarrow 837 \text{ cm}^{-1}$ ). Considering that the P–F vibration of  $\text{PF}_6^-$  was affected by ion association states,<sup>29</sup> this result indicates the electrostatic immobilization of the  $\text{PF}_6^-$  by the positively charged bipyridinium of the TpBpy-COF-Q. In addition, the local chemical environment of  $\text{Li}^+$  within the ASEI layer was investigated using  $^7\text{Li}$  NMR spectroscopy (Figure 2f). The ASEI layer exhibited a narrow width (indicating the enhanced mobility of free  $\text{Li}^+$ )<sup>31,32</sup> and downshift (indicating the dissociation of Li salts) of the singlet  $^7\text{Li}$  peak. To further elucidate this behavior, we performed the saturation recovery measurement (inset of Figure 2f). The ASEI layer exhibited a smaller  $T_1$  value ( $0.47 \text{ s}$ ) than the solidified LE film ( $1.15 \text{ s}$ ), indicating a faster  $\text{Li}^+$  mobility.<sup>20,32</sup> This result was confirmed by analyzing cyclic

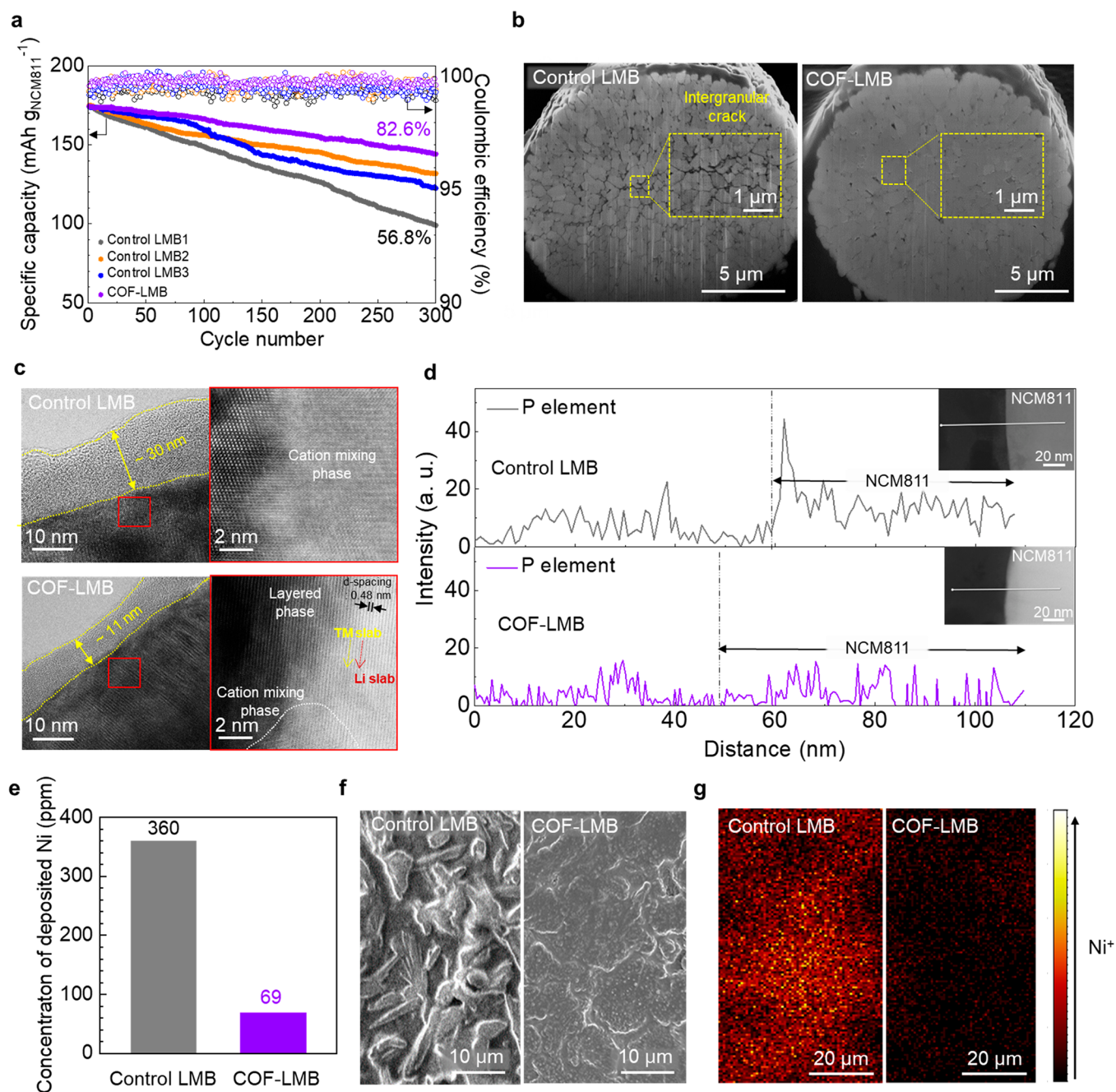


**Figure 3.** Enhancement in the electrochemical performance of LMBs by COF molecular traps. (a) Cycling performance of the COF-LMB (vs control LMBs) at charge/discharge current density of 0.2 C/1.0 C and 45 °C. (b) FIB-SEM, (c) HR-TEM (left), HADDF-STEM images (right), and (d) EDS line analysis of the P element along the depth of the cycled NCM811 particles (after 300 cycles). Insets are the HR-TEM images showing the EDS scan position: control LMB1 (top) and COF-LMB (bottom). (e) Concentration of the Ni deposited on the cycled Li metal anode (obtained from the ICP-OES analysis) after 300 cycles. (f) Surface SEM images of the cycled Li metal anodes (control LMB1 vs COF-LMB) after 300 cycles. (g) TOF-SIMS mapping images of the Ni deposited on the cycled Li metal anodes after 300 cycles.

voltammetry (CV) profiles of Li||Cu asymmetric cells (ASEI-coated Cu vs pristine Cu) (Figure S25).

In addition to the previously described analysis of Li<sup>+</sup> and PF<sub>6</sub><sup>-</sup> in the ASEI layer, the solvation sheath coordination structure was investigated. The LE (Figure 2e) exhibited a characteristic FT-IR peak at 1769 cm<sup>-1</sup>, which was assigned as Li<sup>+</sup>-coordinated carbonates.<sup>31,33</sup> In contrast, the peak of Li<sup>+</sup>-coordinated carbonates was downshifted to 1763 cm<sup>-1</sup>, indicating that the desolvation of Li<sup>+</sup>-coordinated carbonates could be facilitated by the TpBpy-COF-Q in the ASEI layer.

This result was theoretically verified using DFT calculation (Figures S26 and S27).<sup>30</sup>

This advantageous effect of the ASEI layer on the anion immobilization and facile Li<sup>+</sup> desolvation led to an improvement in the Li plating/stripping behavior of the cell at a current density of 1 mA cm<sup>-2</sup> and capacity of 1 mAh cm<sup>-2</sup> (Figure 2g). Moreover, this stable cyclability was still observed even at a higher current density of 5 mA cm<sup>-2</sup> and capacity of 5 mAh cm<sup>-2</sup> (Figure S28). To further elucidate the Li metal stabilization enabled by the ASEI layer, we conducted local electrochemical impedance spectroscopy (LEIS) analysis<sup>34,35</sup>



that can quantitatively identify the uniformity of ionic topology and resistance (Figure 2h). The ASEI-coated Cu exhibited a uniform ionic topology with a low average local resistance ( $138 \Omega \text{ cm}^2$ ) after five Li plating/stripping cycles compared to the pristine Cu, which exhibited an inhomogeneous ionic topology with a relatively high and uneven average local resistance ( $214 \Omega \text{ cm}^2$ ) owing to the interfacial side reactions between the liquid electrolyte (specifically, anions and solvents) and plated Li.<sup>23,34</sup> This result demonstrates that the ASEI layer enables preferential and uniform  $\text{Li}^+$  flow toward the Li metal.

The effect of the on-demand COF molecular traps described above on high-energy-density Li metal full cells was investigated. The TMC cathode was assembled using the ASEI-coated Li metal anode to obtain the COF-LMB. Additionally, three control LMB cells were prepared using the same cell fabrication process: control LMB1 (without any COF molecular traps in the NCM811 cathode and in the ASEI layer of Li metal anode), control LMB2 (with TpBpy-COF in the NCM811 cathode and without TpBpy-COF-Q in the ASEI layer of Li metal anode), and control LMB3 (without TpBpy-COF-Q in the NCM811 cathode and with TpBpy-COF-Q in the ASEI layer of Li metal anode).

The cyclic voltammogram (CV) profiles of the cells showed that the incorporated COF molecular traps allowed the decrease in the gap between the anodic and cathode peak potentials, which indicates the improvement in the redox kinetics at the electrodes (Figure S29). Notably, the COF-LMB exhibited the smallest gap in the peak potential compared to the control LMB cells, verifying the coupled effect of the TpBpy-COF (customized for NCM811 cathode) with the TpBpy-Q-COF (for Li metal anode) as on-demand molecular traps.

The COF-LMB and control LMBs were cycled at a charge/discharge current density of 0.2 C/1.0 C at 45 °C, where the temperature of 45 °C was chosen to accelerate the detrimental effects caused by the dissolution of TM ions.<sup>10,36</sup> The control LMBs suffered from capacity degradation with cycling, which was more pronounced for the control LMB1 (56.8% after 300 cycles). Meanwhile, the control LMB3 showed a relatively rapid decline in the cycling retention after 100 cycles. This result indicates the beneficial effects of the TpBpy-COF-Q in the ASEI layer of the Li metal anode on the cycling performance during the early stage of cycling. However, the absence of the TpBpy-COF in the NCM811 cathode of the control LMB3 may result in a relatively rapid capacity degradation during the later stage of cycling. Further studies will be conducted to elucidate this cycling behavior. In contrast, the COF-LMB exhibited stable capacity retention (82.6% after 300 cycles) (Figures 3a and S30). This enhanced cyclability of the COF-LMB was verified by analyzing its EIS spectra (Figure S31). The COF-LMB cell mitigated the growth in the cell impedance compared to the control LMB1 (Table S6). Furthermore, the COF-LMB exhibited higher discharge capacities over a wide range of discharge current densities (0.2–8.0 C) compared to the control LMBs (Figure S32).

To elucidate this difference in the cyclability, a postmortem analysis of the cells was conducted after 300 cycles. During cycling, liquid electrolytes penetrate into NCM811 particles, thus triggering the disruption of their layered structure and generation of a NiO phase. Consequently, this resulted in the anisotropic change of the lattice parameter of the NCM811 particles and the generation of cracks, which resulted in the deterioration of the performance of the NCM811 cathode.<sup>10,32</sup>

Figure 3b shows that the cycled NCM811 particles of the COF-LMB maintained their structural integrity, whereas those of the control LMB1 suffered from severe cracking and disruption. This result demonstrates that the TpBpy-COF in the TMC cathode played a crucial role in the prevention of the interfacial side reactions between the NCM811 particles and liquid electrolyte owing to its ability to suppress the  $\text{Ni}^{2+}$ -induced solvent decomposition (Figure S13).

The  $\text{Ni}^{2+}$  dissolution-induced structural transformation of the NCM811 from a layered to a NiO-like rock-salt phase is known to deteriorate its electrochemical performance.<sup>3,8–10</sup> The high-resolution TEM (HR-TEM) and high-angle annular dark field scanning transmission electron microscopy (HAADF-STEM) images of the cycled NCM811 particles revealed the presence of a thick CEI layer ( $>30 \text{ nm}$ ) and rock-salt phase in the control LMB1 (Figure 3c, top). In contrast, the layered structure with  $d$ -spacing of 0.48 nm was stably preserved in the cycled NCM811 of the COF-LMB, together with the formation of a thin CEI layer ( $\sim 11 \text{ nm}$ ) and NiO-like rock-salt phase ( $<5 \text{ nm}$ ) (Figure 3c, bottom). In addition, the anion decomposition-derived byproducts<sup>32,37</sup> were investigated by conducting EDS line analysis along the depth of the cycled NCM811. Compared to the control LMB1, a negligible amount of P element was observed at the COF-LMB (Figure 3d), which may due to the suppression in the catalytic  $\text{Ni}^{2+}$ -driven parasitic side reactions<sup>38</sup> with  $\text{PF}_6^-$  of the liquid electrolyte. This result demonstrates the beneficial effect of COF molecular traps on the  $\text{Ni}^{2+}$  chelation.

The CEI layers were further characterized using XPS and time-of-flight secondary ion mass spectroscopy (TOF-SIMS) analysis. A characteristic peak assigned to  $\text{NiF}_2$  (684.6 eV) byproducts,<sup>3,8</sup> which are formed by unwanted interfacial side reactions between NCM811 and electrolytes, was observed in the XPS F 1s spectra (Figure S33) of the cycled NCM811 (after 300 cycles) of the control LMB1. This XPS result is consistent with the depth profiling of TOF-SIMS measurement (Figure S34). The cycled NCM811 particles of the COF-LMB exhibited the lower fragments of byproducts (such as  $\text{C}_2\text{HO}^-$ ,  $\text{PO}_2^-$ , and  $\text{NiF}_3^-$ ) stemming from electrolyte decomposition and TM ion dissolution<sup>8–11,36</sup> compared to those of the control LMB1. In addition to the detrimental effect on the structural stability of cycled NCM811 described previously, the dissolved TM ions (e.g.,  $\text{Ni}^{2+}$ ) tend to migrate toward the Li metal anode and form passivation layers.<sup>8</sup> The ICP-OES analysis (Figure 3e) revealed that the COF-LMB (69 ppm) suppressed the Li metal contamination induced by the deposition of dissolved  $\text{Ni}^{2+}$  compared to the control LMB1 (360 ppm). In addition, solvent molecules were often decomposed by the reduction of the dissolved  $\text{Ni}^{2+}$  at the Li metal anode,<sup>8,11,38</sup> resulting in the formation of randomly distributed passivation layers (Figure 3f, left). In contrast, a relatively smooth and clean morphology was observed at the Li metal anode of the COF-LMB (Figure 3e, right), indicating the mitigation of catalytic decomposition of solvents. These results were further verified by TOF-SIMS analysis, which revealed a significant decrease in the  $\text{Ni}^{2+}$ -triggered byproducts at the Li metal anode of the COF-LMB (Figure 3g).

In addition to thin Li metal anodes, high areal-mass-loading cathodes are required to enable high-energy-density LMB full cells.<sup>3,4,34</sup> In this study, we prepared various TMC cathodes as a function of the areal mass loadings (Figure S35). Neither structural disruption nor delamination was observed even at a high areal mass loading of  $31.6 \text{ mg cm}^{-2}$  (corresponding to an

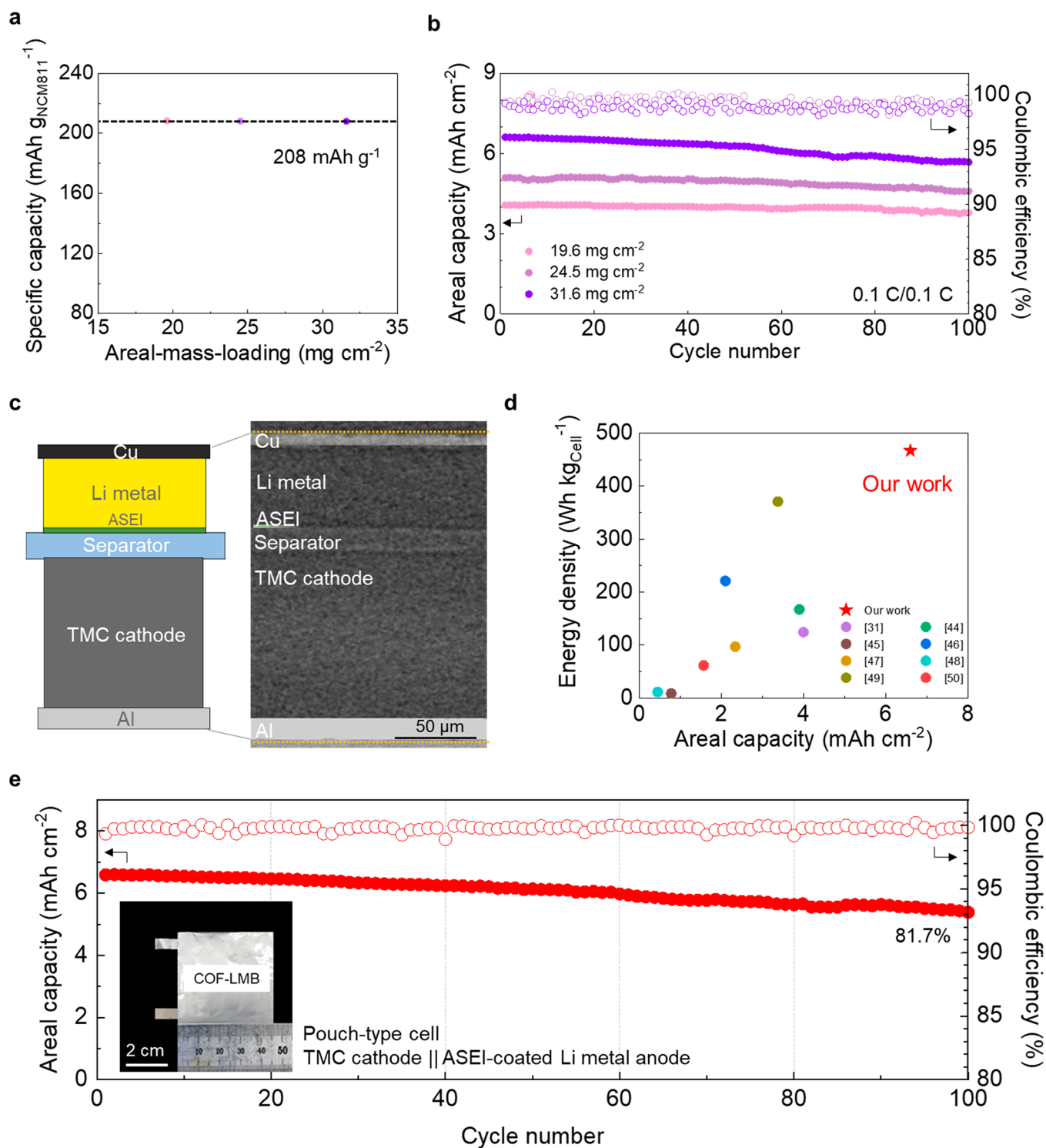


Figure 4. High-energy-density COF-LMB full cells with high-mass-loading TMC cathodes. (a) Specific capacity (based on the weight of NCM811 particles) of the TMC cathodes and (b) cycling performance of the TMC cathodes and as a function of the areal mass loading at a charge/discharge current density of 0.1 C/0.1 C. (c) Schematic illustration and X-ray CT image of the pouch-type COF-LMB full cell (TMC cathode (areal capacity of 6.6 mA h cm<sup>-2</sup>)||ASEI-coated Li metal anode (areal capacity of 10.0 mA h cm<sup>-2</sup>, N/P = 1.5). (d) Cycling performance of the pouch-type COF-LMB full cell at a charge/discharge current rate of 0.1 C (= 0.66 mA cm<sup>-2</sup>)/0.1 C and voltage range of 3.0–4.4 V under a limited amount of electrolyte (E/C ratio of 2.3 g Ah<sup>-1</sup>). Inset is a photograph of the pouch-type cell (46 × 44 mm<sup>2</sup> in size). (e) Gravimetric energy densities of the cells as a function of the areal capacity (COF-LMB full cell (this study) vs previously reported full cells with porous crystalline frameworks (such as COF and MOF). Details on the references are provided in Table S8.

areal capacity of 6.6 mA h cm<sup>-2</sup>). Achieving theoretical capacities of cathode materials is still a major difficulty in the development of high-mass-loading cathodes.<sup>34,39</sup> In this study,

the TMC cathodes exhibited a nearly full utilization of the theoretical specific capacity (~210 mA h g<sub>NCM811</sub><sup>-1</sup>)<sup>3</sup> of NCM811 over the entire areal-mass-loading range examined

herein (Figures 4a and S36). Moreover, the obtained TMC cathodes exhibited a stable cycling performance at a high charge cutoff voltage of 4.4 V (Figure 4b). This achievement in the electrochemical performance of the areal-mass-loading TMC cathodes can be attributed to the advantageous effect of the TpBpy-COF molecular traps, which were uniformly distributed along the thickness of the TMC cathode, as previously shown in Figure S17.

To explore the practical applicability of the COF-LMB, a pouch-type full cell ( $46 \times 44 \text{ mm}^2$  in size) was fabricated, and its cell performance was investigated over a voltage range of 3.0–4.4 V. The pouch-type full cell consisted of the TMC cathode (areal capacity of  $6.6 \text{ mAh cm}^{-2}$ )||ASEI-coated Li metal anode (areal capacity of  $10.0 \text{ mAh cm}^{-2}$ , negative (N)/positive (P) capacity ratio = 1.5). The cross-sectional morphology of the prepared full cell was characterized using X-ray computed tomography (CT), revealing the well-defined and intimate interfacial contact between the component layers (Figure 4c). In addition, we observed that the amount of liquid electrolyte in the cell was set as  $2.3 \text{ g Ah}^{-1}$  by considering a preferred amount of electrolyte ( $<3.0 \text{ g Ah}^{-1}$  for practical high-energy-density full cells).<sup>4,34</sup> A commercially accessible conventional liquid electrolyte (1 M  $\text{LiPF}_6$  in EC/EMC = 3/7 (v/v) with 10 wt % FEC, 1 wt % VC) was employed to explore the feasibility of the COF molecular traps for practical applications compared to the specially designed liquid electrolytes<sup>12,13</sup> with unusual solvents/salts/additives and complicated composition ratios. The pouch-type full cell exhibited a discharge capacity of  $208 \text{ mAh g}^{-1}$  (Figure S37), which was almost consistent with the result shown in Figure 4a.

To enable the commercial feasibility of LMB full cells, high energy densities should be secured while ensuring high areal capacities. The gravimetric/volumetric energy densities of the pouch-type full cell (herein, the packaging substance was excluded for a fair comparison with the results of previous studies) were estimated to reach  $466.7 \text{ Wh kg}_{\text{cell}}^{-1}/1370.1 \text{ Wh L}_{\text{cell}}^{-1}$  at a high areal capacity of  $6.6 \text{ mAh cm}^{-2}$  (Table S7), which far exceeded those reported in previous studies on full cells with porous crystalline frameworks, such as COF and MOF (Figure 4d and Table S8).<sup>31,40–46</sup> In addition, the energy densities (including the packaging substances) of the pouch-type full cell were estimated to be  $300.6 \text{ Wh kg}_{\text{cell}}^{-1}/715.7 \text{ Wh L}_{\text{cell}}^{-1}$  (Table S7). We expect that the cell energy density values can be further increased by introducing a multicell stack configuration that allows the reduction of the weight/volume portion of the packaging substances in the resulting full cells. Under the constrained cell condition (i.e., high areal capacity, low N/P ratio, and limited amount of the commercially available liquid electrolyte), the pouch-type full cell exhibited a stable cycling retention of 81.7% at 100 cycles (Figure 4e). This result demonstrates the viability of the COF molecular traps in achieving a practical high-energy-density LMB full cell.

In summary, we demonstrated the electrostatic COFs as on-demand molecular traps to regulate electrostatic interactions between charged molecules, in which these COF molecular traps were designed to simultaneously fulfill the heterogeneous electrochemical requirements of thin Li metal anodes and high-capacity cathodes for practical high-energy-density LMBs. The synthesized TpBpy-COF and TpBpy-COF-Q were incorporated in an NCM811 cathode to chelate TM ions and in an ASEI layer to immobilize anions of liquid electrolytes, respectively. These COF molecular traps allowed

the dipole-dipole interaction with the  $\text{Li}^+$  solvation sheath of the liquid electrolytes, thereby lowering the desolvation energy and suppressing the solvent decomposition. Owing to these combined effects of the TpBpy-COF and TpBpy-COF-Q molecular traps, the resulting COF-LMB exhibited an almost full utilization of the theoretical specific capacity of NCM811 and stable cycling performance over a wide range of areal mass loadings. Notably, the pouch-type COF-LMB achieved high gravimetric/volumetric energy densities ( $466.7 \text{ Wh kg}_{\text{cell}}^{-1}/1370.1 \text{ Wh L}_{\text{cell}}^{-1}$ ) under the constrained cell condition, which exceeded those of previously reported cells based on porous crystalline frameworks such as COFs and MOFs. This COF molecular trap strategy opens a new route toward electrode design and shows potential as a platform technology for the advancement of emerging high-energy-density metal (including Zn, Mg, and Al) batteries as well as LMBs.

## ■ ASSOCIATED CONTENT

### Supporting Information

The Supporting Information is available free of charge at <https://pubs.acs.org/doi/10.1021/acsenerylett.3c00600>.

Synthesis of the TpBpy-COF and TpBpy-COF-Q, structural and physicochemical characterizations, fabrication and electrochemical characterization of the TMC cathode and ASEI-coated Li metal anode, electrochemical characterization of the COF-LMB full cells, calculation of energy densities, density functional theory (DFT) calculations, molecular electrostatic potential and calculation of Gibb's free energy of formation, desolvation energy calculations, anion-immobilizing calculation (PDF)

## ■ AUTHOR INFORMATION

### Corresponding Authors

Jia Guo – State Key Laboratory of Molecular Engineering of Polymers, Department of Macromolecular Science, Fudan University, Shanghai 200433, China; [orcid.org/0000-0003-4869-9992](https://orcid.org/0000-0003-4869-9992); Email: [guojia@fudan.edu.cn](mailto:guojia@fudan.edu.cn)

Dong-Hwa Seo – School of Energy and Chemical Engineering, Ulsan National Institute of Science and Technology (UNIST), Ulsan 44919, Republic of Korea; Email: [dseo@unist.ac.kr](mailto:dseo@unist.ac.kr)

Sang-Young Lee – Department of Chemical and Biomolecular Engineering, Yonsei University, Seoul 03722, Republic of Korea; [orcid.org/0000-0001-7153-0517](https://orcid.org/0000-0001-7153-0517); Email: [syleek@yonsei.ac.kr](mailto:syleek@yonsei.ac.kr)

### Authors

Kyeong-Seok Oh – Department of Chemical and Biomolecular Engineering, Yonsei University, Seoul 03722, Republic of Korea

Sodam Park – School of Energy and Chemical Engineering, Ulsan National Institute of Science and Technology (UNIST), Ulsan 44919, Republic of Korea

Jae-Seung Kim – School of Energy and Chemical Engineering, Ulsan National Institute of Science and Technology (UNIST), Ulsan 44919, Republic of Korea

Ying Yao – State Key Laboratory of Molecular Engineering of Polymers, Department of Macromolecular Science, Fudan University, Shanghai 200433, China



Jung-Hui Kim – School of Energy and Chemical Engineering,  
Ulsan National Institute of Science and Technology  
(UNIST), Ulsan 44919, Republic of Korea

Complete contact information is available at:

<https://pubs.acs.org/10.1021/acsenerylett.3c00600>

### Author Contributions

K.-S.O., S.P., and J.-S.K. contributed equally. K.-S.O., S.P., and S.-Y.L. designed all electrochemical experiments and analyzed the results. J.-S.K. and D.-H.S. designed and performed all theoretical calculations. Y.Y. synthesized the covalent organic framework. J.-H.K. designed the LEIS analysis. K.-S.O., S.P., and J.-S.K. prepared the manuscript. J.G., D.-H.S., and S.-Y.L. revised the manuscript critically. All authors have given approval for the final version of the manuscript.

### Notes

The authors declare no competing financial interest.

## ACKNOWLEDGMENTS

This work was supported by the Basic Science Research Program (2018M3D1A1058744, 2021R1A2B5B03001615, and 2022M3J1A1085397) through the National Research Foundation of Korea (NRF) grant by the Korean Government (MSIT) and the Korea Institute of Energy Technology Evaluation and Planning (KETEP) grant funded by the Korea government (MOTIE) (20221B1010003B). The computational resources were provided by KITS (KSC-2021-CRE-0337 to D.-H.S.).

## REFERENCES

- (1) Schmuck, R.; Wagner, R.; Höppl, G.; Placke, T.; Winter, M. Performance and cost of materials for lithium-based rechargeable automotive batteries. *Nat. Energy* **2018**, *3*, 267–278.
- (2) Larcher, D.; Tarascon, J. M. Towards greener and more sustainable batteries for electrical energy storage. *Nat. Chem.* **2015**, *7*, 19–29.
- (3) Li, W.; Erickson, E. M.; Manthiram, A. High-nickel layered oxide cathodes for lithium-based automotive batteries. *Nat. Energy* **2020**, *5*, 26–34.
- (4) Ren, X.; Zou, L.; Cao, X.; Engelhard, M. H.; Liu, W.; Burton, S. D.; Lee, H.; Niu, C.; Matthews, B. E.; Zhu, Z.; Wang, C.; Arey, B. W.; Xiao, J.; Liu, J.; Zhang, J.-G.; Xu, W. Enabling high-voltage lithium-metal batteries under practical conditions. *Joule* **2019**, *3*, 1662–1676.
- (5) Xu, W.; Wang, J.; Ding, F.; Chen, X.; Nasybulin, E.; Zhang, Y.; Zhang, J.-G. Lithium metal anodes for rechargeable batteries. *Energy Environ. Sci.* **2014**, *7*, 513–537.
- (6) Cheng, X.-B.; Zhang, R.; Zhao, C.-Z.; Zhang, Q. Toward safe lithium metal anode in rechargeable batteries: A review. *Chem. Rev.* **2017**, *117*, 10403–10473.
- (7) Lin, D.; Liu, Y.; Cui, Y. Reviving the lithium metal anode for high-energy batteries. *Nat. Nanotechnol.* **2017**, *12*, 194–206.
- (8) Kim, J.; Ma, H.; Cha, H.; Lee, H.; Sung, J.; Seo, M.; Oh, P.; Park, M.; Cho, J. A highly stabilized nickel-rich cathode material by nanoscale epitaxy control for high-energy lithium-ion batteries. *Energy Environ. Sci.* **2018**, *11*, 1449–1459.
- (9) Manthiram, A. A reflection on lithium-ion battery cathode chemistry. *Nat. Commun.* **2020**, *11*, 1550.
- (10) Jung, S.-K.; Gwon, H.; Hong, J.; Park, K.-Y.; Seo, D.-H.; Kim, H.; Hyun, J.; Yang, W.; Kang, K. Understanding the degradation mechanisms of  $\text{LiNi}_{0.5}\text{Co}_{0.2}\text{Mn}_{0.3}\text{O}_2$  cathode material in lithium ion batteries. *Adv. Energy Mater.* **2014**, *4*, 1300787.
- (11) Li, T.; Yuan, X.-Z.; Zhang, L.; Song, D.; Shi, K.; Bock, C. Degradation mechanisms and mitigation strategies of nickel-rich NMC-based lithium-ion batteries. *Electrochem. Energy Rev.* **2020**, *3*, 43–80.
- (12) Weber, R.; Genovese, M.; Louli, A. J.; Hames, S.; Martin, C.; Hill, I. G.; Dahn, J. R. Long cycle life and dendrite-free lithium morphology in anode-free lithium pouch cells enabled by a dual-salt liquid electrolyte. *Nat. Energy* **2019**, *4*, 683–689.
- (13) Yu, Z.; Wang, H.; Kong, X.; Huang, W.; Tsao, Y.; Mackanic, D. G.; Wang, K.; Wang, X.; Huang, W.; Choudhury, S.; Zheng, Y.; Amanchukwu, C. V.; Hung, S. T.; Ma, Y.; Lomeli, E. G.; Qin, J.; Cui, Y.; Bao, Z. Molecular design for electrolyte solvents enabling energy-dense and long-cycling lithium metal batteries. *Nat. Energy* **2020**, *5*, 526–533.
- (14) Han, J.-G.; Lee, J. B.; Cha, A.; Lee, T. K.; Cho, W.; Chae, S.; Kang, S. J.; Kwak, S. K.; Cho, J.; Hong, S. Y.; Choi, N.-S. Unsymmetrical fluorinated malonateborate as an amphoteric additive for high-energy-density lithium-ion batteries. *Energy Environ. Sci.* **2018**, *11*, 1552–1562.
- (15) Xu, G.; Pang, C.; Chen, B.; Ma, J.; Wang, X.; Chai, J.; Wang, Q.; An, W.; Zhou, X.; Cui, G.; Chen, L. Prescribing functional additives for treating the poor performances of high-voltage (5 V-class)  $\text{LiNi}_{0.5}\text{Mn}_{1.5}\text{O}_4/\text{MCMB}$  Li-ion batteries. *Adv. Energy Mater.* **2018**, *8*, 1701398.
- (16) Hu, Y.; Waymouth, L. J.; Haslam, C.; Yang, X.; Lee, S.-H.; Jin, Y.; Zhang, W. Covalent organic framework based lithium-ion battery: Fundamental, design and characterization. *EnergyChem.* **2021**, *3*, 100048.
- (17) Liang, X.; Tian, Y.; Yuan, Y.; Kim, Y. Ionic Covalent Organic Frameworks for Energy Devices. *Adv. Mater.* **2021**, *33*, 2105647.
- (18) Du, Y.; Yang, H.; Whiteley, J. M.; Wan, S.; Jin, Y.; Lee, S.-H.; Zhang, W. Ionic Covalent Organic Frameworks with Spiroborate Linkage. *Angew. Chem., Int. Ed.* **2016**, *55*, 1737–1741.
- (19) Liang, X.; Tian, Y.; Yuan, Y.; Kim, Y. Ionic Covalent Organic Frameworks for Energy Devices. *Angew. Chem., Int. Ed.* **2021**, *33*, 2105647.
- (20) Jeong, K.; Park, S.; Jung, G. Y.; Kim, S. H.; Lee, Y.-H.; Kwak, S. K.; Lee, S.-Y. Solvent-free, single lithium-ion conducting covalent organic frameworks. *J. Am. Chem. Soc.* **2019**, *141*, 5880–5885.
- (21) Cho, S.-K.; Kim, H.-I.; An, J.-W.; Jung, K.; Bae, H.; Kim, J. H.; Yim, T.; Lee, S.-Y. Printable solid electrolyte interphase mimic for antioxidative lithium metal electrodes. *Adv. Funct. Mater.* **2020**, *30*, 2000792.
- (22) Mi, Z.; Zhou, T.; Weng, W.; Unruangsri, J.; Hu, K.; Yang, W.; Wang, C.; Zhang, K. A. I.; Guo, J. Stable radical cation-containing covalent organic frameworks exhibiting remarkable structure-enhanced photothermal conversion. *Angew. Chem., Int. Ed.* **2021**, *60*, 9642–9649.
- (23) Mi, Z.; Yang, P.; Wang, R.; Unruangsri, J.; Yang, W.; Wang, C.; Guo, J. Stable radical cation-containing covalent organic frameworks exhibiting remarkable structure-enhanced photothermal conversion. *J. Am. Chem. Soc.* **2019**, *141*, 14433–14442.
- (24) Cho, Y.-G.; Jung, S.-H.; Joo, S. H.; Jeon, Y.; Kim, M.; Lee, K. M.; Kim, S.; Park, J. M.; Noh, H. K.; Kim, Y.-S.; Hong, J.-E.; Jeon, S.-I.; Kim, T.; Kwak, S. K.; Kong, H.; Song, H.-K. A metal-ion-chelating organogel electrolyte for Le Chatelier depression of  $\text{Mn}^{3+}$  disproportionation of lithium manganese oxide spinel. *J. Mater. Chem. A* **2018**, *6*, 22483–22488.
- (25) Dalapati, S.; Jin, S.; Gao, J.; Xu, Y.; Nagai, A.; Jiang, D. An Azine-Linked Covalent Organic Framework. *J. Am. Chem. Soc.* **2013**, *135*, 17310–17313.
- (26) Vyas, V. S.; Haase, F.; Stegbauer, L.; Savasci, G.; Podjaski, F.; Ochsenfeld, C.; Lotsch, B. V. A tunable azine covalent organic framework platform for visible light-induced hydrogen generation. *Nat. Commun.* **2015**, *6*, 8508.
- (27) Dong, Y.; Demeaux, J.; Zhang, Y.; Xu, M.; Zhou, L.; MacIntosh, A. D.; Lucht, B. L. Improving the performance at elevated temperature of high voltage graphite/ $\text{LiNi}_{0.5}\text{Mn}_{1.5}\text{O}_4$  cells with added lithium catechol dimethyl borate. *J. Electrochem. Soc.* **2017**, *164*, A128.
- (28) Ogihara, N.; Kawauchi, S.; Okuda, C.; Itou, Y.; Takeuchi, Y.; Ukyo, Y. Theoretical and experimental analysis of porous electrodes

for lithium-ion batteries by electrochemical impedance spectroscopy using a symmetric cell. *J. Electrochem. Soc.* **2012**, *159*, A1034–A1039.

(29) Li, Y.; Qi, Y. Energy landscape of the charge transfer reaction at the complex Li/SEI/electrolyte interface. *Energy Environ. Sci.* **2019**, *12*, 1286–1295.

(30) Wen, Y.; Ding, J.; Yang, Y.; Lan, X.; Liu, J.; Hu, R.; Zhu, M. Introducing NO<sup>3-</sup> into carbonate-based electrolytes via covalent organic framework to incubate stable interface for Li-metal batteries. *Adv. Funct. Mater.* **2022**, *32*, 2109377.

(31) Cho, S.-K.; Oh, K.-S.; Shin, J. C.; Lee, J. E.; Lee, K. M.; Cho, J.; Lee, W. B.; Kwak, S. K.; Lee, M.; Lee, S.-Y. Anion-rectifying polymeric single lithium-ion conductors. *Adv. Funct. Mater.* **2022**, *32*, 2107753.

(32) Oh, K.-S.; Kim, J.-H.; Kim, S.-H.; Oh, D.; Han, S.-P.; Jung, K.; Wang, Z.; Shi, L.; Su, Y.; Yim, T.; Yuan, S.; Lee, S.-Y. Single-ion conducting soft electrolytes for semi-solid lithium metal batteries enabling cell fabrication and operation under ambient conditions. *Adv. Energy Mater.* **2021**, *11*, 2101813.

(33) Chen, H.; Tu, H.; Hu, C.; Liu, Y.; Dong, D.; Sun, Y.; Dai, Y.; Wang, S.; Qian, H.; Lin, Z.; Chen, L. Cationic covalent organic framework nanosheets for fast Li-ion conduction. *J. Am. Chem. Soc.* **2018**, *140*, 896–899.

(34) Kim, J.-H.; Kim, J.-M.; Cho, S.-K.; Kim, N.-Y.; Lee, S.-Y. Redox-homogeneous, gel electrolyte-embedded high-mass-loading cathodes for high-energy lithium metal batteries. *Nat. Commun.* **2022**, *13*, 2541.

(35) Huang, V. M.; Wu, S.-L.; Orazem, M. E.; Pébère, N.; Tribollet, B.; Vivier, V. Local electrochemical impedance spectroscopy: A review and some recent developments. *Electrochim. Acta* **2011**, *56*, 8048–8057.

(36) Zhan, C.; Wu, T.; Lu, J.; Amine, K. Dissolution, migration, and deposition of transition metal ions in Li-ion batteries exemplified by Mn-based cathodes - a critical review. *Energy Environ. Sci.* **2018**, *11*, 243–257.

(37) Delp, S. A.; Borodin, O.; Olguin, M.; Eisner, C. G.; Allen, J. L.; Jow, T. R. Importance of reduction and oxidation stability of high voltage electrolytes and additive. *Electrochim. Acta* **2016**, *209*, 498–510.

(38) Wang, C.; Xing, L.; Vatamanu, J.; Chen, Z.; Lan, G.; Li, W.; Xu, K. Overlooked electrolyte destabilization by manganese (II) in lithium-ion batteries. *Nat. Commun.* **2019**, *10*, 3423.

(39) Kuang, Y.; Chen, C.; Kirsch, D.; Hu, L. Thick electrode batteries: principles, opportunities, and challenges. *Adv. Energy Mater.* **2019**, *9*, 1901457.

(40) Chen, D.; Liu, P.; Zhong, L.; Wang, S.; Xiao, M.; Han, D.; Huang, S.; Meng, Y. Covalent organic frameworks with low surface work function enabled stable lithium anode. *Small* **2021**, *17*, 2101496.

(41) Wang, W.; Yang, Z.; Zhang, Y.; Wang, A.; Zhang, Y.; Chen, L.; Li, Q.; Qiao, S. Highly stable lithium metal anode enabled by lithiophilic and spatial-confined spherical-covalent organic framework. *Energy Storage Mater.* **2022**, *46*, 374–383.

(42) Jiang, G.; Li, K.; Yu, F.; Li, X.; Mao, J.; Jiang, W.; Sun, F.; Dai, B.; Li, Y. Robust artificial solid-electrolyte interfaces with biomimetic ionic channels for dendrite-free Li metal anodes. *Adv. Energy Mater.* **2021**, *11*, 2003496.

(43) Chang, Z.; Qiao, Y.; Deng, H.; Yang, H.; He, P.; Zhou, H. A stable high-voltage lithium-ion battery realized by an in-built water scavenger. *Energy Environ. Sci.* **2020**, *13*, 1197–1204.

(44) Li, X.; Tian, Y.; Shen, L.; Qu, Z.; Ma, T.; Sun, F.; Liu, X.; Zhang, C.; Shen, J.; Li, X.; Gao, L.; Xiao, S.; Liu, T.; Liu, Y.; Lu, Y. Electrolyte interphase built from anionic covalent organic frameworks for lithium dendrite suppression. *Adv. Funct. Mater.* **2021**, *31*, 2009718.

(45) Zhao, Z.; Chen, W.; Impeng, S.; Li, M.; Wang, R.; Liu, Y.; Zhang, L.; Dong, L.; Unruangsri, J.; Peng, C.; Wang, C.; Namuangruk, S.; Lee, S.-Y.; Wang, Y.; Lu, H.; Guo, J. Covalent organic framework-based ultrathin crystalline porous film: manipulating uniformity of fluoride distribution for stabilizing lithium metal anode. *J. Mater. Chem. A* **2020**, *8*, 3459–3467.

(46) Jerng, S. E.; Chang, B.; Shin, H.; Kim, H.; Lee, T.; Char, K.; Choi, J. W. Pyrazine-linked 2D covalent organic frameworks as coating material for high-nickel layered oxide cathodes in lithium-ion batteries. *ACS Appl. Mater. Interfaces* **2020**, *12*, 10597–10606.